



## Full Length Article

# A rationally designed flexible self-healing system with a high performance supercapacitor for powering an integrated multifunctional sensor



Min Su Kim<sup>a</sup>, Jung Wook Kim<sup>b</sup>, Junyeong Yun<sup>b</sup>, Yu Ra Jeong<sup>b</sup>, Sang Woo Jin<sup>a</sup>, Geumbee Lee<sup>a</sup>, Hanchan Lee<sup>b</sup>, Dong Sik Kim<sup>b</sup>, Kayeon Keum<sup>b</sup>, Jeong Sook Ha<sup>a,b,\*</sup>

<sup>a</sup> KU-KIST Graduate School of Converging Science and Technology, Korea University, 145 Anam-ro, Seongbuk-gu, Seoul 02841, Republic of Korea

<sup>b</sup> Department of Chemical and Biological Engineering, Korea University, 145 Anam-ro, Seongbuk-gu, Seoul 02841, Republic of Korea

## ARTICLE INFO

## Keywords:

Self-healing electronics  
Poly(vinyl alcohol)/borax/agarose/NaNO<sub>3</sub>  
hydrogel electrolyte  
High performance supercapacitor  
Multifunctional sensor  
All-in-one system

## ABSTRACT

We report on the fabrication of a rationally designed self-healing and flexible all-in-one system. Using a vacuum filtration method, an integrated system consisting of a planar supercapacitor and a multifunctional sensor is fabricated with gold nanosheet (AuNS) interconnections. A fast and reversible self-healing hydrogel based on the diol-ester bonding between poly(vinyl alcohol) (PVA) and borax is synthesized, and its mechanical stability is enhanced with the additional hydrogen bonding between PVA and agarose. Using an electrolyte of PVA/borax/agarose/NaNO<sub>3</sub> and an electrode consisting of multiwalled carbon nanotubes (MWCNTs) coated on an AuNS current collector, a high-performance self-healing flexible planar supercapacitor is fabricated. The multifunctional sensor is made of MWCNTs with a zinc oxide nanowire composite. Both the supercapacitor and sensor recover their performance from bisectational damage via physical contact with a water supply. The self-healing supercapacitor shows mechanical stability for bending deformation even after repetitive self-healing cycles. Furthermore, the integrated system exhibits self-healing performance through stable sensing of NO<sub>2</sub> gas and UV light using the stored energy in the supercapacitor after recovery from repetitive bisection of the sensor. This work demonstrates the high potential of our rationally designed flexible self-healing all-in-one system in high-performance wearable devices with high durability and longevity.

## 1. Introduction

Recently, multifunctional wearable electronic devices have attracted extensive attention as one of the next generation core technologies. Wearable devices are required to have mechanical stability under various deformations due to body movement and the ability to obtain precise information on biosignals as well as environmental signals, such as hazardous gases and harmful UV light. Along with the dramatic advances in the development of high-performance flexible/stretchable sensor devices, high-performance energy storage devices for powering of integrated sensor device in the form of all-in-one system have been actively investigated [1–4]. In addition, visual display of the electrical sensing signal via integration of an electrochromic display or quantum dot light emitting diode array has recently attracted attention [5–8]. Furthermore, extensive research on self-healable wearable devices has recently increased because the self-healing ability can increase the lifetime of wearable electronic devices. These devices can recover their original performances even after repeated damage during everyday

usage.

Self-healing electronic devices have been fabricated based on combining conductive materials, such as metal nanowires, conducting polymers and carbon-based materials, with self-healing polymers. The self-healing polymers studied to date include polyvinyl alcohol (PVA) [9–11], vinyl silica cross-linked polyacrylic acid [12], dicyclopentadiene [13], TiO<sub>2</sub>-doped polymers [14], carboxylate polyurethane [15,16], and β-cyclodextrin (β-CD) complex [17–19]. Self-healing electronic devices, such as chemical/mechanical sensors, electrochromic devices and electroluminescence devices have been reported [20–23]. In addition, research has been actively conducted to produce self-healing electrochemical capacitors (ECs) with active materials such as multiwalled carbon nanotubes (MWCNTs) or activated carbon as electrodes and conductive self-healing electrolytes based on the abovementioned self-healing polymers [24–27].

Despite the considerable progress in developing self-healable devices, there are still limitations that hinder their wide applications. Most of the previously reported self-healing applications are based on

\* Corresponding author at: KU-KIST Graduate School of Converging Science and Technology, Korea University, 145 Anam-ro, Seongbuk-gu, Seoul 02841, Republic of Korea.

E-mail address: [jeongsha@korea.ac.kr](mailto:jeongsha@korea.ac.kr) (J.S. Ha).

<https://doi.org/10.1016/j.apsusc.2020.146018>

Received 6 January 2020; Received in revised form 19 February 2020; Accepted 7 March 2020

Available online 14 March 2020

0169-4332/ © 2020 Elsevier B.V. All rights reserved.

the demonstration of a single functional device. However, integration of multiple self-healing functional devices in a self-healing all-in-one system is required for practical daily utilization. A fully self-healable electronic system consisting of an electrocardiogram sensor, a strain sensor and a light-emitting capacitor was only reported [28]. Other than various functional devices, integration of energy storage devices such as batteries and supercapacitors for powering an entire system is also essential. However, most of the previously reported self-healing energy storage devices were designed in a stacked structure, which make them hard to integrate with other devices on a single wearable substrate. Also, self-healing supercapacitors studied earlier rarely have current collectors, which could deteriorate the charge transport performance of the supercapacitor.

In designing a self-healing supercapacitor, it is challenging to synthesize a highly conductive hydrogel electrolyte while maintaining its mechanical stability as well as self-healing property. Among various self-healing polymers, PVA has been widely used for fabricating self-healing devices due to its electrochemical and chemical stability, easy processability and biocompatibility. Thus, PVA has been frequently used for the synthesis of electrolytes. PVA-based electrolytes mainly include acids [29,30], bases [31,32] or other inorganic salts [33,34] dissolved in deionized water. However, these electrolytes often have poor self-healing efficiency, even though they contain sufficient hydroxyl groups (–OH) from PVA. This poor efficiency is attributed to the presence of inorganic ions from the acids, bases, or salts in the electrolyte because these ions can hinder the formation of hydrogen bond between the PVA chains and water molecules [35]. This can cause aggregation of the PVA chains due to intermolecular hydrogen bonding, which significantly reduces the chain mobility that is essential for self-healing [36,37]. Thus, the application of PVA-based electrolytes to self-healing devices is limited due to their poor healing efficiency and poor tolerance to salt. Chemical modification of PVA chains by grafting functional molecules such as acrylic acid or N, N, N-trimethyl-1-(oxiran-2-yl) methanaminium chloride has been suggested to reduce the aggregation of PVA chains in the presence of ions [10,38]. However, this strategy often requires complex chemical reactions or additional processes such as purification or neutralization.

In this study, we devise a facile fabrication process for a flexible self-healing sensor system with an integrated supercapacitor via a vacuum filtration technique. In particular, we suggest a novel strategy to enhance the self-healing efficiency as well as the electrochemical performance of the supercapacitor. Both mechanical stability and high ionic conductivity with the excellent self-healing properties of the hydrogel electrolyte, PVA/borax/agarose/ $\text{NaNO}_3$ , are obtained by a systematic study on the role of the agarose content and various electrolyte ions in the self-healing efficiency of the hydrogel polymer. Highly conductive and flexible AuNSs as a current collector also contribute to enhancing the electrochemical performance of the supercapacitor. A self-healing multifunctional sensor is fabricated with a patterned channel consisting of MWCNTs and ZnO nanowires (NWs) to detect both  $\text{NO}_2$  gas and UV light. Via integration of a planar supercapacitor and multifunctional sensor using AuNS interconnections onto a single PVA/agarose film, a self-healing all-in-one system is fabricated that can detect UV and  $\text{NO}_2$  with a sensor driven by the energy stored in the planar supercapacitor. Both the supercapacitor and the sensor recover their device performance after complete bisection and subsequent physical contact with a water supply for a short time.

This work clearly suggests that our rationally designed self-healing all-in-one device is widely applicable to soft wearable electronics with high durability and longevity.

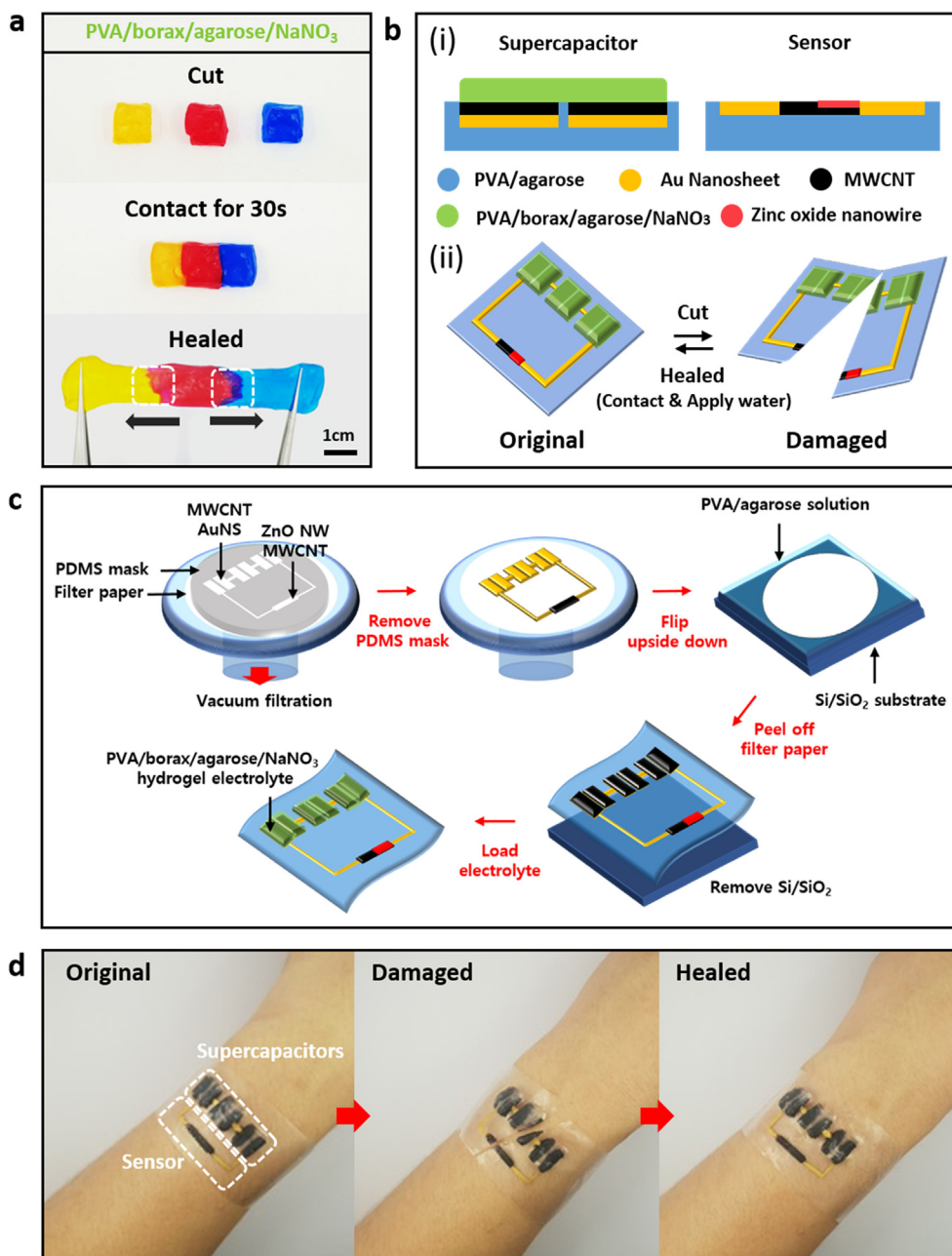
## 2. Results and discussion

Fig. 1a shows photographs taken of the PVA/borax/agarose/ $\text{NaNO}_3$  hydrogel electrolyte during the processes of cutting, physical contact, and confirmation of mechanical recovery under the ambient air

environment to examine the self-healing property. Each bisected hydrogel was first contacted under a small applied pressure and then contacted for 30 s without any external force. The healed hydrogel was stretchable, demonstrating the excellent self-healing property of the hydrogel. Optical microscopy images in Fig. S1 also confirm the fast self-healing of the hydrogel electrolyte. In Fig. 1b (i), the detailed structures of the fabricated self-healing planar supercapacitor and multifunctional sensor are schematically shown. The thickness of the fabricated MWCNT layer, AuNS layer and PVA/agarose substrate was estimated to be 60, 20, and 100  $\mu\text{m}$ , respectively, from the cross-sectional scanning electron microscopy (SEM) images in Fig. S2. Fig. 1b (ii) schematically illustrates the healing process of the all-in-one system consisting of three serially connected supercapacitors, the multifunctional sensor, and AuNS interconnections. A detailed fabrication process is schematically illustrated in Fig. 1c. Supercapacitor electrodes were fabricated by transferring vacuum-filtrated MWCNT and AuNS films onto the PVA/agarose substrate using filter paper. The PDMS mask was designed to make the desired electrode pattern for the supercapacitor, sensor and interconnections. The dispersion of MWCNTs and AuNSs was drop-cast to form a percolated network on the filter paper. After the patterning process, the PDMS mask was removed. The filter paper with patterned electrodes was placed on a PVA/agarose solution drop-cast on top of a silicon ( $\text{Si}/\text{SiO}_2$ ) substrate and then dried on a 55  $^\circ\text{C}$  hot plate. After 4 h of drying, the filter paper was slowly peeled off. The transferred pattern formed a conductive percolated network of MWCNTs/AuNSs. The hydrogel electrolyte was simply loaded on top of the electrodes, including the interfaces. The multifunctional sensor was fabricated with MWCNTs and ZnO NW composites embedded in the same PVA/agarose substrate, and the AuNS interconnections were also transferred in the same way to integrate the supercapacitors and the sensor, forming an all-in-one sensor system. Photographs taken of the device attached on a wrist during the damage/self-healing process are shown in Fig. 1d.

The self-healing mechanism of the PVA/borax/agarose hydrogel is schematically illustrated in Fig. 2a with molecular structures of the individual components. Borax molecules form tetrahydroxy borate anions ( $\text{B}(\text{OH})_4^-$ ) in aqueous solution, which enable fast and reversible self-healing of the hydrogels through a dynamic covalent cross-linking reaction with the hydroxyl groups of the adjacent PVA [39,40]. However, the fabricated PVA/borax hydrogel has a weak physical/mechanical property due to a single type of bonding. To enhance the mechanical strength, agarose was added to the hydrogel to form an additional network due to additional hydrogen bonding with PVA [41,42]. Hydrogels without agarose could not retain their original shape over time, while those with agarose contents above 2 wt% could reduce their fluidity to maintain the shape, as demonstrated in Fig. S3. To confirm that the component materials used in the hydrogel were well mixed, Fourier transform infrared (FT-IR) spectra of PVA, agarose, PVA/agarose and PVA/borax/agarose composites were obtained, as shown in Fig. S4. All materials showed a similar peak near 3330  $\text{cm}^{-1}$  and a peak at 1645  $\text{cm}^{-1}$ , which represent the stretching and bending vibrations of hydroxyl (O–H) groups. Additionally, the common peaks, though slightly shifted, near 2950  $\text{cm}^{-1}$ , 2890  $\text{cm}^{-1}$ , 1410  $\text{cm}^{-1}$  and 1330  $\text{cm}^{-1}$  correspond to the stretching, bending, wagging and rocking modes of C–H bonds, respectively. The peak at 1100  $\text{cm}^{-1}$  is assigned to the out-of-plane vibration of C–O, and the peak at 820  $\text{cm}^{-1}$  corresponds to the stretching vibration of C–C bonds [43–48]. Additionally, peaks at 1365  $\text{cm}^{-1}$ , 1064  $\text{cm}^{-1}$  and 850  $\text{cm}^{-1}$  correspond to the stretching relaxation of B–O–C, asymmetric stretching vibration of B–O and symmetric stretching of B–O, respectively, confirming crosslinking between PVA and borax as well as the presence of a borax network in the hydrogel [49].

Fig. 2b shows the strain-stress curves of the PVA/borax/agarose hydrogel taken as the agarose content was varied from 0 to 3 wt%. Here, the 2 mm thick hydrogel film was cut into strips of 20 mm  $\times$  5 mm. With the increasing agarose content, the maximum



**Fig. 1.** (a) Photograph showing the self-healing process of the fabricated self-healable hydrogel electrolyte. (b) Schematic illustration of the fabricated self-healable all-in-one electronic system with detailed structures. (i) Cross-sectional scheme of the fabricated supercapacitor and sensor. (ii) Self-healing process of the all-in-one system. (c) Schematic illustration of the fabrication process. (d) Photographs of the integrated device attached to skin during the cutting and healing process.

tensile stress increased due to the formation of more hydrogen bonds with PVA. The elastic modulus ( $E$ ) also showed the same tendency and was 6.41 kPa for the hydrogel without agarose and increased to 9.37, 14.36 and 20.27 kPa for agarose contents of 1, 2, and 3 wt%, respectively. The elastic modulus was calculated by the following Eq. (1):

$$E = \frac{\sigma}{\epsilon} = \frac{F \times L_0}{A \times \Delta L} \quad (1)$$

where  $L_0$ ,  $\Delta L$ ,  $A$  and  $F$  represent the initial length, length change, cross-sectional area of the hydrogel, and applied force, respectively. These results clearly indicate that the addition of agarose leads to an improvement in the mechanical strength of the hydrogel.

To further understand the influence of agarose on the properties of the hydrogel, the elastic modulus and healing efficiency histograms with the variation in the agarose content are shown in Fig. 2c. Here, the

healing efficiency is based on the recovery of the strain at break. In all cases, the healing efficiency is over 96%, especially over 98% when the agarose content is less than 3 wt%. Since pure agarose gel has no healing ability, we expect that the addition of more than a certain amount of agarose may affect the healing ability of the hydrogel. Thus, we used the 2 wt% hydrogel, which was moderately stable and flexible, throughout the remaining experiments. Fig. 2d shows the strain-stress curves for the hydrogel electrolyte with various added electrolyte materials. The elastic modulus and healing efficiency histograms are also summarized in Fig. 2e. The concentration of each electrolyte solution was kept at 1 M. All measurements were performed 30 min after application of 1 ml electrolyte solution to the PVA/borax/agarose hydrogel. As shown in Fig. S5, the addition of acid ( $H_3PO_4$ ) completely disrupts the intermolecular bonding network of the hydrogel, making the hydrogel more like a liquid and resulting in a dramatic decrease in

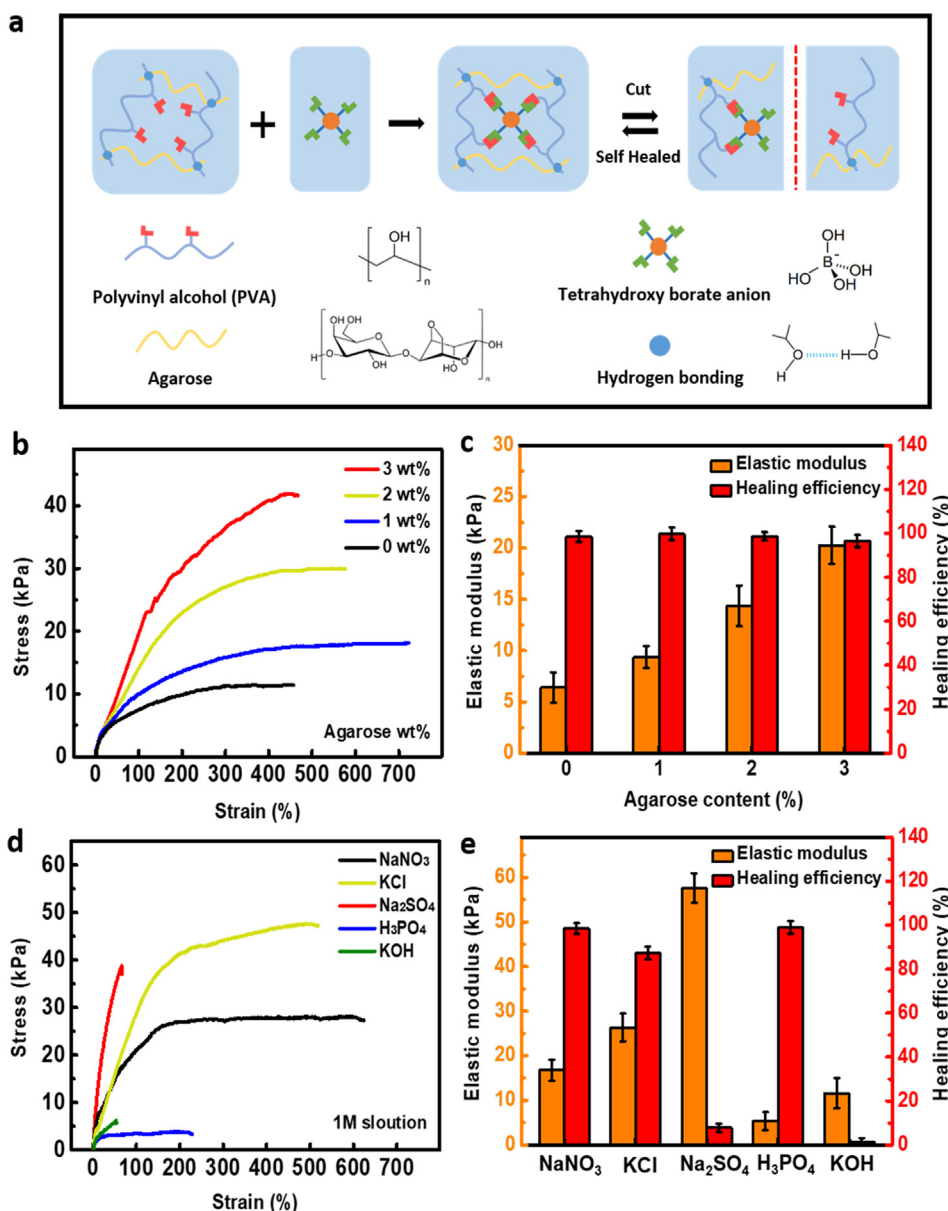


**Fig. 2.** (a) Schematic illustration of the self-healing mechanism of the fabricated PVA/borax/agarose hydrogel. (b) Strain-stress curves of the hydrogel with different contents of agarose. (c) Measured elastic modulus and self-healing efficiency of the hydrogel with various agarose contents. (d) Strain-stress curves of the hydrogel with 2 wt% of agarose after treatment with various electrolytes. (e) Measured elastic modulus and self-healing efficiency of the hydrogel treated with various electrolytes.

the elastic modulus. Although the addition of base (KOH) did not affect the appearance of the hydrogel, it completely removed the self-healing ability of the hydrogel. Both hydrogels treated with KCl and Na<sub>2</sub>SO<sub>4</sub> became opaque white, and the elastic modulus increased to 26.3 and 57.6 kPa, respectively. The self-healing efficiency also decreased to 87.2% and 7.8%, respectively.

These results can be explained in terms of the Hofmeister effect. The Hofmeister effect is a theory that ions can affect the behavior of other solutes, such as macromolecules, in aqueous solutions. The Hofmeister series is the classification of ions in order of their ability to salt out or salt in polymers [50,51]. Here, kosmotropic and chaotropic ions are categorized based on their ability to alter the hydrogen bonding network of water. According to the Hofmeister series, both KCl and Na<sub>2</sub>SO<sub>4</sub> have kosmotropic characteristics. They promote hydrogen bonding between water molecules, weakening the bonding between PVA chains and water molecules and lowering the polymer solubility. As a result, the PVA chains aggregate through intermolecular interactions with

other adjacent PVA chains, resulting in a salting-out effect in which the water and polymers are separated [52]. SO<sub>4</sub><sup>-</sup> ions tend to be more kosmotropic than Cl<sup>-</sup> ions. For this reason, the dehydration and decrease in healing efficiency was more severe in the Na<sub>2</sub>SO<sub>4</sub> treated hydrogels than the KCl treated hydrogels.

To solve this problem, we introduced NaNO<sub>3</sub> as a novel electrolyte material based on the abovementioned theory. NO<sub>3</sub><sup>-</sup>, the anion of NaNO<sub>3</sub>, is a strong chaotropic ion. Chaotropic ions rarely disturb the hydrogen bonding between water molecules and PVA chains. Therefore, unlike other electrolyte materials, when NaNO<sub>3</sub> was added to the hydrogel, it was possible to maintain a high ionic conductivity and capacitance for the supercapacitor while also maintaining the mechanical properties and excellent self-healing ability of the original hydrogel. According to the theory, the effect of Na<sup>+</sup> on the self-healing efficiency is negligible and anions appear to have a larger effect than cations [53]. Information on the strength of various kosmotropic and chaotropic ions is given in Fig. S6.

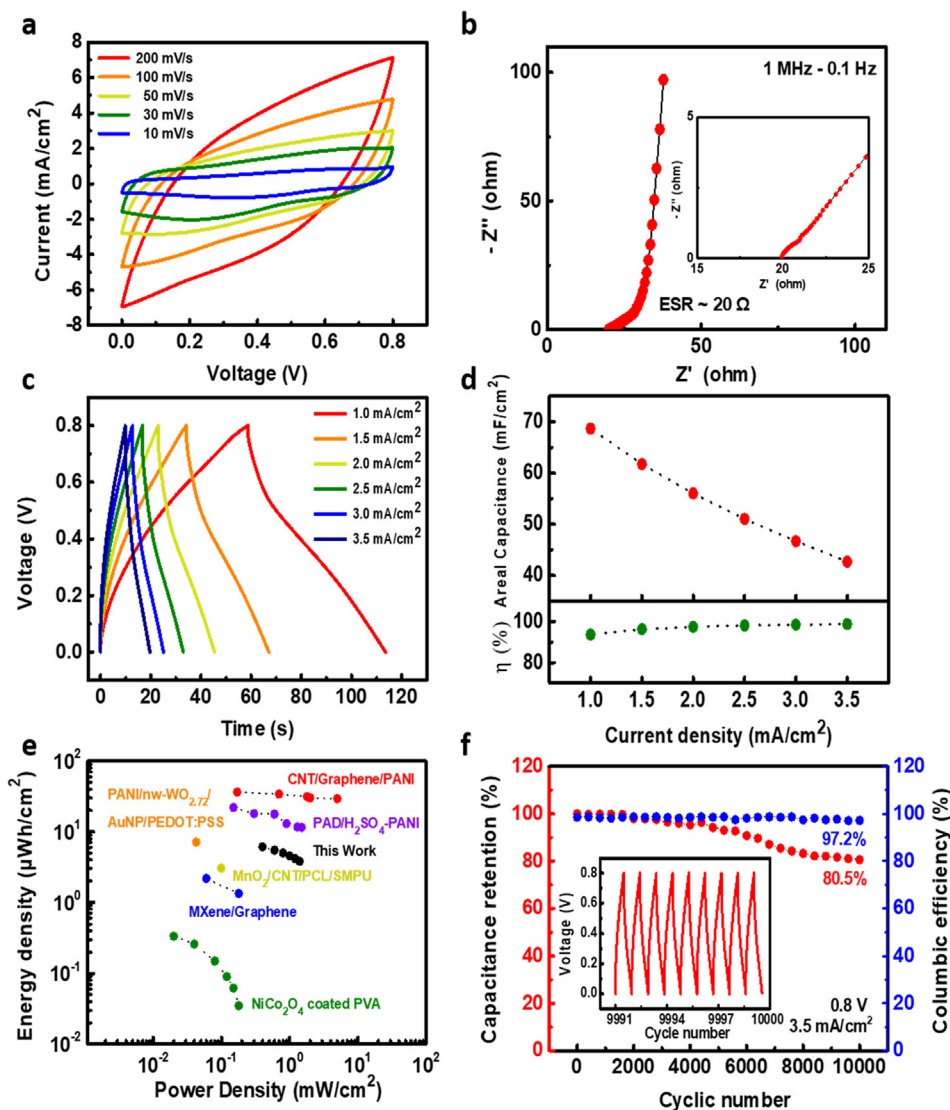


**Fig. 3.** Electrochemical performance of the self-healable planar supercapacitor with MWCNT/AuNS electrodes and PVA/borax/agarose/ $\text{NaNO}_3$  hydrogel electrolyte. (a) Cyclic voltammetry (CV) curves taken at scan rates from  $10 \text{ mV s}^{-1}$  to  $200 \text{ mV s}^{-1}$ . (b) Nyquist plot of the supercapacitor. Inset shows an enlarged plot at high frequency region. (c) Galvanostatic charge-discharge (GCD) curves taken at current densities from  $1.0$  to  $3.5 \text{ mA cm}^{-2}$ . (d) Areal capacitance and columbic efficiency ( $\eta$ ) calculated from the GCD curves. (e) Ragone plot of the supercapacitor compared with those of other previously reported self-healable supercapacitors. (f) Cyclic stability of the fabricated supercapacitor. The inset shows GCD curves taken during the last 9 cycles.

Next, the electrochemical performance of the fabricated planar supercapacitor was measured. Fig. 3a shows the cyclic voltammetry (CV) curves taken at various scan rates from  $10$  to  $200 \text{ mV s}^{-1}$  with symmetric shapes. The Nyquist plot of the electrochemical impedance spectroscopy (EIS) spectra measured at frequencies from  $1 \text{ MHz}$  to  $0.1 \text{ Hz}$  in Fig. 3b shows that the angle between the plot and the x-axis is close to  $90$  degrees indicating electrical double layer capacitor (EDLC) behavior [54]. In this case, the value corresponding to the x intercept,  $\sim 20 \Omega$ , is the equivalent series resistance (ESR) or cell internal resistance ( $R_b$ ), which corresponds to the resistance of the components of the supercapacitor, such as the electrode, current collector, and electrolyte. The charge transfer resistance ( $R_{ct}$ ) value was measured to be  $1 \Omega$ , which is negligible. Equivalent circuit model used for fitting the EIS spectra of the supercapacitor cell is shown in Fig. S7. Fig. 3c shows the galvanostatic charge-discharge (GCD) curves measured at various current densities. From those GCD curves, the areal capacitance ( $C_A$ ) can be calculated using Eq. (2):

$$C_A = \frac{I \times \Delta t}{\Delta V \times A} \quad (2)$$

where  $I$ ,  $\Delta t$ ,  $\Delta V$  and  $A$  represent the current density, discharge time, operation voltage and cell active area, including the interface of  $500 \mu\text{m}$  between electrodes, respectively. The transferred electrodes have two rectangular structures with a length of  $1 \text{ cm}$  and a width of  $0.4 \text{ cm}$ . The

maximum areal capacitance was calculated to be  $68.7 \text{ mF cm}^{-2}$  at a current density of  $1.0 \text{ mA cm}^{-2}$ , and it gradually decreased with increasing current density, resulting in a value of  $42.7 \text{ mF cm}^{-2}$  at  $3.5 \text{ mA cm}^{-2}$ . Columbic efficiency remained above  $94\%$  at all current densities as shown in Fig. 3d. The areal energy density ( $E_A$ ) and areal power density ( $P_A$ ) of the fabricated supercapacitor can also be calculated by Eqs. (3) and (4), respectively.

$$E_A = \frac{C_A \times \Delta V^2}{7200} \quad (3)$$

$$P_A = \frac{E_A \times 3600}{\Delta t} \quad (4)$$

The maximum power and energy density values were calculated to be  $1.4 \text{ mW cm}^{-2}$  and  $6.1 \mu\text{Wh cm}^{-2}$ , respectively. Compared to previously reported self-healing supercapacitors, our fabricated supercapacitor exhibits excellent performance as shown in the Ragone plot in Fig. 3e [15,24,55–58]. In Table S1, the electrochemical performance of our fabricated self-healing supercapacitor is compared with that of other previously reported ones. Such high performance is attributed to the high concentration of ions in our self-healing hydrogel electrolyte. As mentioned above, it was possible to obtain a high concentration of ions using  $\text{NaNO}_3$  in our hydrogel, whereas hydrogels with only a much lower concentration of other previously reported acids, bases, or inorganic salts could be formed. The addition of ions above a critical

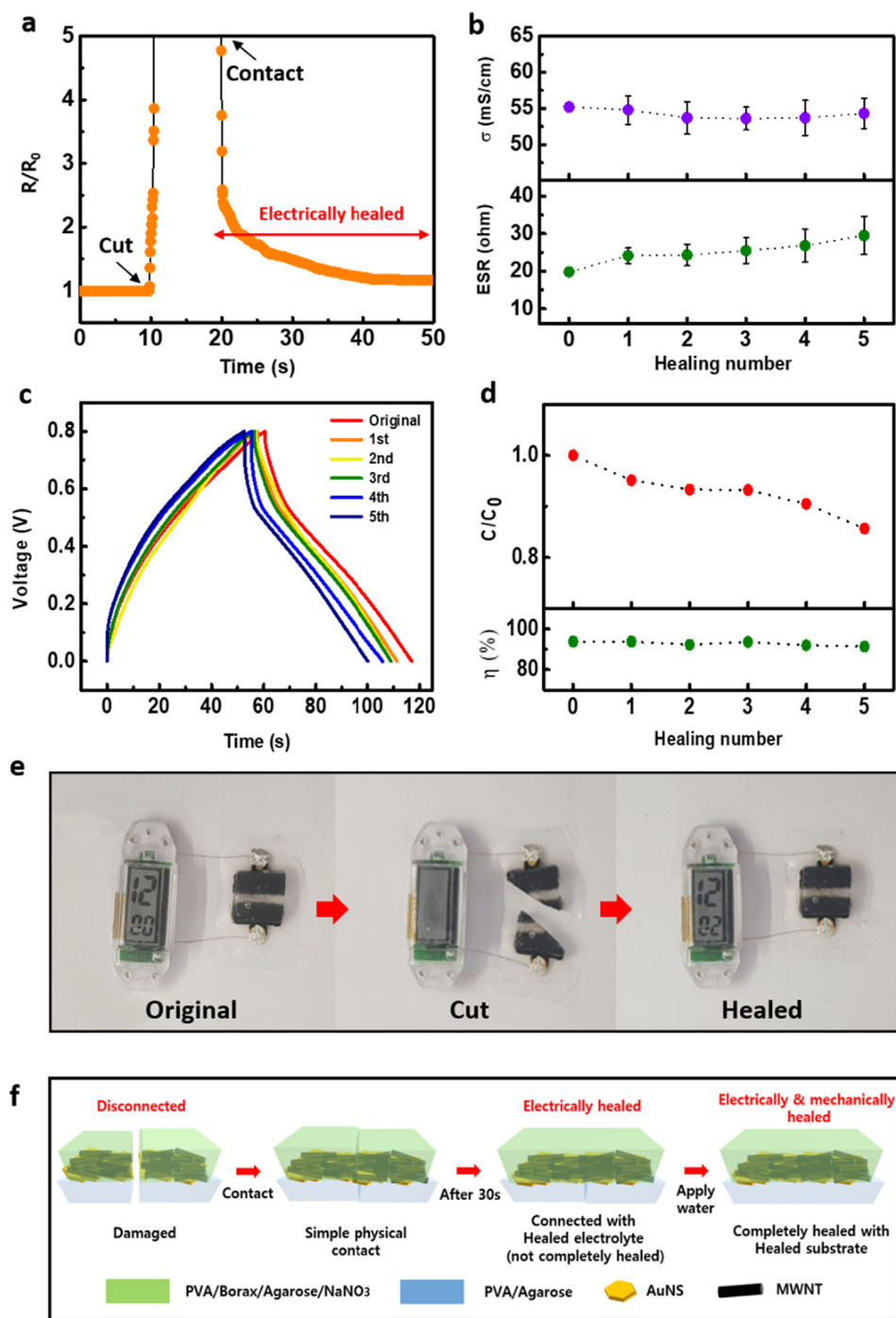


Fig. 4. (a) Time-dependent  $R/R_0$  graph of the supercapacitor electrode with electrolyte measured after complete bisection and physical contact of the two pieces. (b) Ionic conductivity of the hydrogel electrolyte (top) and ESR value of the fabricated supercapacitor (bottom) with respect to self-healing cycles. (c) GCD curves taken over 5 cycles of self-healing at a current density of  $1.0 \text{ mA cm}^{-2}$ . (d) Normalized capacitance and columbic efficiency with self-healing cycles calculated from the GCD curves. (e) Liquid crystal display (LCD) integrated with the self-healable supercapacitor during the damage and self-healing processes. (f) Schematic illustration of the self-healing process of the fabricated supercapacitor.

concentration can lower the mechanical and self-healing ability of the electrolyte, causing a significant decrease in the self-healing property of the whole device. The presence of a highly conductive AuNS current collector is also attributed to the high performance of the supercapacitor, while most of the previously reported supercapacitors do not have current collectors tightly connected with the active materials. The resistance of our AuNS current collector as well as the interconnections is measured to be  $\sim 3 \Omega$ . Additionally, the output voltage and the charge/discharge time can be controlled via serial and parallel connections of multiple supercapacitors, as clearly exhibited in Fig. S8. Fig. 3f presents the changes in capacitance over 10,000 repetitive charge/discharge cycles at a current density of  $3.5 \text{ mA cm}^{-2}$ , and the inset shows GCD curves taken over the last 9 cycles. After 10,000 cycles of charge/discharge, the supercapacitor maintained 80.5% of its initial

performance, and the columbic efficiency was maintained at over 97.2%. During the measurements, the supercapacitor was sealed with parafilm in a circular petri dish with a diameter of 55 mm to minimize the effect of water evaporation on the performance.

In Fig. 4, the electrochemical performance of our supercapacitor after cycles of damage/healing is measured. Fig. 4a shows the time-dependent normalized resistance change of the supercapacitor electrode with the electrolyte measured after complete bisection and physical reconnection of the two pieces. The resistance of the electrode gradually returns to the original value when the completely bisected pieces are physically reconnected, forming an electrical pathway. Fig. 4b shows the change in ionic conductivity of the hydrogel electrolyte for 5 damage/healing cycles (top) and the change in the ESR value of the whole supercapacitor according to the healing cycles

(bottom). The ionic conductivity ( $\sigma$ ) of the prepared hydrogel electrolyte can be calculated by the following Eq. (5):

$$\sigma = \frac{1000 \times d}{R \times A} \quad (5)$$

where  $R$ ,  $A$  and  $d$  refer to the bulk resistance of the hydrogel electrolyte, electrode area coated with electrolyte, and the distance between the electrodes, respectively. The electrolyte was sandwiched between two gold plates. The area of the electrode was  $1.0 \text{ cm}^2$ , the distance between two plates was  $0.2 \text{ cm}$ . The bulk resistance of the hydrogel was  $3.6 \Omega$  and it was measured by EIS in the range of  $1 \text{ MHz}$  to  $100 \text{ Hz}$ . The ionic conductivity of the prepared hydrogel electrolyte was calculated to be  $55.2 \text{ mS cm}^{-1}$  and it was almost maintained at the initial value after 5 healing cycles. After 5 cycles of damage/healing, the ESR of the supercapacitor increased from  $19.8 \Omega$  to  $29.5 \Omega$ , which was attributed to the increase in the contact resistance at the healed area of the electrodes and penetration of the surrounding polymer into the conductive network of the MWCNTs/AuNSs. Fig. 4c shows the GCD curves of the supercapacitor according to the healing cycles, indicating gradual degradation. The normalized capacitance ( $C/C_0$ ) and the coulombic efficiency with increasing number of healing cycles are shown in Fig. 4d. After 5 self-healing cycles, the capacitance and the coulombic efficiency were maintained 85.6% and 91% of the initial values, respectively. With this fabricated supercapacitor, a liquid crystal display (LCD) could be driven. Upon bisection of the supercapacitor, the LCD was turned off but turned on again after connecting the bisected pieces together, as demonstrated in Fig. 4e.

From these experimental results, we propose the self-healing mechanism of our fabricated supercapacitor, as schematically illustrated in Fig. 4f. Since the percolated network of the conducting nanomaterials of MWCNTs and AuNSs is embedded in the self-healing hydrogel of PVA/agarose and covered with the self-healing electrolyte of PVA/borax/agarose/ $\text{NaNO}_3$ , the mechanical and the electrical properties of the supercapacitor electrode can be recovered due to the self-healing ability of the hydrogel. Although the thickness of each AuNS is tens of nanometers, the sheet structure has a lateral dimension of tens of micrometers. Thus, an electrical pathway is formed by surface-to-surface contact. The SEM image and the energy dispersive spectrum taken of the hexagonal AuNS are shown in Fig. S9. In particular, the MWCNTs/AuNSs covered with the self-healing hydrogel electrolyte recover the original electrical pathway by effectively connecting the AuNS percolated network as the electrolyte hydrogel heals. When the supercapacitor is damaged, both the electrical connection and mechanical connection can be damaged. After connecting the damaged areas with each other, the electrical path can be reconnected via simple physical contact, as shown in Fig. 4a. However, mechanical self-healing of the electrode is not perfect because the underlying self-healing polymer substrate requires a water supply. Although the electrical pathway is regenerated through simple physical contact, it is unstable under deformation such as bending. Thus, supplying water to the contacted area of the substrate can result in mechanical recovery in addition to electrical recovery by the merging the self-healing polymer substrate matrix. Such a self-healing process is fully completed within 30 min. Fig. S10 is the optical microscopy image showing the self-healed area after complete bisection across the electrolyte and the MWCNTs/AuNSs electrode.

The mechanical stability of the fabricated self-healing supercapacitors during bending deformation with various bending radii down to  $1.5 \text{ mm}$  was investigated, as shown in Fig. 5a. Here, bending radius and radius of curvature are used in the same sense, which is reciprocal of the curvature as shown in Fig. S11. The bending radius was measured by using ImageJ software. The CV curves taken at a scan rate of  $100 \text{ mV s}^{-1}$  show a slight but insignificant decrease in the capacitance under bending deformation in Fig. 5b. Such a negligible degradation of the electrochemical performance with bending was also observed in the GCD curves taken at  $1.0 \text{ mA cm}^{-2}$  in Fig. 5c. The EIS

plot and ionic conductivity changes of the hydrogel electrolyte under various bending are shown in Fig. S12. Although the conductivity of the hydrogel electrolyte was changed under bending deformation, it did not significantly affect the actual capacitance of the supercapacitor. After repetitive bending at a bending radius of  $3.6 \text{ mm}$  for up to 500 cycles, the supercapacitor still retained 95.2% of the initial capacitance. After 500 bending cycles, the supercapacitor was bisected and self-healed through physical contact with a water supply. For the self-healed supercapacitor, GCD curves were obtained under repetitive bending at a bending radius of  $3.6 \text{ mm}$ . As shown in Fig. 5d, the self-healed supercapacitor exhibits a gradual decrease in capacitance, reaching 90.1% of the initial capacitance after a total of 1000 bending cycles. The inset shows the GCD curves taken from the supercapacitor before bending and after the 1000th bending cycle, signifying no noticeable degradation even after bending deformation of the self-healed device after complete bisection.

Using the vacuum filtration patterning method, a self-healing multifunctional sensor for detecting both  $\text{NO}_2$  gas and UV light was also fabricated on the PVA/agarose substrate. The sensor channel was made via transfer of vacuum-filtrated MWCNT film and covering over half the area of the MWCNT channel with ZnO NW film. The MWCNT-only channel is expected to detect  $\text{NO}_2$  gas, while the ZnO-covered MWCNTs detect UV light. The SEM image, EDS and XPS spectra of ZnO NWs deposited on patterned MWCNTs are shown in Fig. S13. In the XPS spectrum, Zn  $2p_{1/2}$  and Zn  $2p_{3/2}$  peaks are observed at  $1020.5 \text{ eV}$  and  $1043.5 \text{ eV}$  with a spin-orbit splitting value of  $23.0 \text{ eV}$ , which corresponds to  $\text{Zn}^{2+}$  (left) [59]. The O  $1s$  peak can be fitted with two Gaussian peaks at  $531.2$  and  $529.1 \text{ eV}$ , corresponding to the OH group on the surface of the ZnO and  $\text{O}^{2-}$  ions in the wurtzite structure of ZnO with Zn-O bonding, respectively (right) [60,61].

Fig. 6a schematically illustrates the sensing mechanism of hazardous  $\text{NO}_2$  gas (left) and UV light (right) by using the fabricated multifunctional sensor. In ambient air, semiconducting MWCNTs exhibit p-type conduction behavior.  $\text{NO}_2$  has a dipole that strongly attracts electrons. Upon adsorption on the surface of the p-MWCNTs, the adsorbed  $\text{NO}_2$  exists as  $\text{NO}_2^-$  ions due to extraction of electrons from the electron-hole (e-h) pair of the MWCNTs. As a result, additional holes are generated in the MWCNT channel to increase the current with increasing  $\text{NO}_2$  exposure [62–64]. On the other hand, UV light can be detected by ZnO NWs. In an ambient air environment,  $\text{O}_2$  is adsorbed on the ZnO surface in the form of  $\text{O}_2^-$ . Exposure to UV light with energy higher than the bandgap of ZnO ( $E_g = 3.37 \text{ eV}$ ) generates e-h pairs in ZnO. Then, the photogenerated holes combine with  $\text{O}_2^-$  to form  $\text{O}_2$ , which can desorb from the surface. As a result, photogenerated electrons flow through the metallic MWCNT channel and increase the photocurrent [65,66]. The scheme in the middle illustrates our self-healing all-in-one system consisting of a  $\text{NO}_2$ /UV sensor and three serially connected supercapacitors integrated by using AuNS interconnections. In this system, the sensor is driven by the stored energy of the fully charged integrated supercapacitor without any wire connection to an external power supply.

Fig. 6b and d show the current changes detected by the sensor after repeated exposure to  $10 \text{ ppm NO}_2$  (gas on:  $4 \text{ s}$ , gas off:  $36 \text{ s}$ ) and  $365 \text{ nm UV light}$  (UV on:  $12 \text{ s}$ , UV off:  $30 \text{ s}$ ). Upon exposure to  $\text{NO}_2$  gas and UV, an increase in the current was observed in both cases, as expected based on the sensing mechanism in Fig. 6a. To confirm that the supercapacitor can be used as an integrated energy storage device for the sensor, the sensing behavior was compared with that driven by the external power supply with a constant bias voltage of  $1.5 \text{ V}$ . As the number of cycles increased, however, the base current  $I_{\text{air}}$  increased for  $\text{NO}_2$  sensing with an external power supply, as shown in Fig. 6b. This is attributed to incomplete desorption of residual  $\text{NO}_2$  from the MWCNTs with repetitive exposure to  $\text{NO}_2$  gas [67,68]. However, as the exposure time increased, both the on- and off- currents gradually decreased for the sensor driven by the supercapacitor array, due to the discharge of the integrated supercapacitor. Nonetheless, the sensing performance

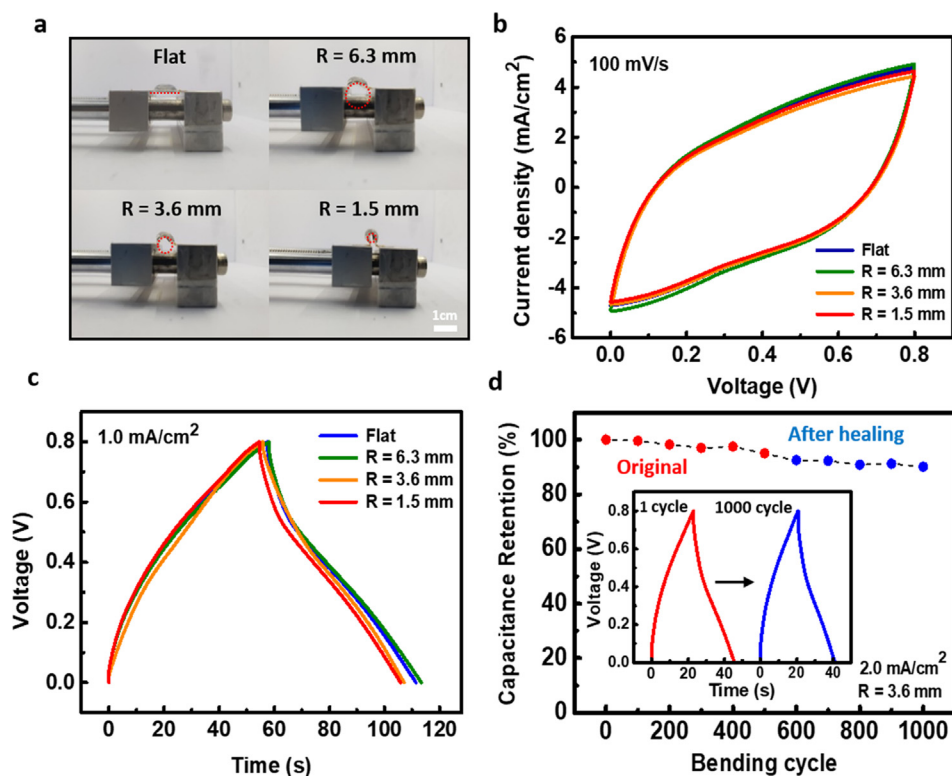


Fig. 5. (a) Photographs of the supercapacitor under bending deformation with various bending radii. (b) CV curves taken under bending deformation at a scan rate of  $100 \text{ mV s}^{-1}$ . (c) GCD curves taken under bending deformation at a current density of  $1.0 \text{ mA cm}^{-2}$ . (d) Capacitance retention during the repetitive bending cycles at a bending radius of 3.6 mm before (red) and after (blue) self-healing. The inset shows the GCD curves obtained after the 1st and 1000th bending cycles. (For interpretation of the references to colour in this figure legend, the reader is referred to the web version of this article.)

remained almost the same as that of the sensor driven at a constant bias voltage, confirming the stable operation of our integrated multifunctional sensor.

The sensitivity ( $S$ ) of the sensor is defined as  $S = I_{\text{on}} - I_{\text{off}}/I_{\text{off}}$ , where  $I_{\text{on}}$  ( $I_{\text{gas}}$ ) is the current flow upon exposure to  $\text{NO}_2$  gas or UV light and  $I_{\text{off}}$  ( $I_{\text{air}}$ ) is the current without UV light or  $\text{NO}_2$ . Fig. 6c shows the change in the normalized UV sensitivity ( $S/S_0$ ) with respect to the number of self-healing cycles. Here,  $S_0$  and  $S$  are the sensitivity before and after self-healing, respectively. On the bottom, a change in the current with exposure to  $\text{NO}_2$  gas for the sensors before and after repeated self-healing is shown. After five repeated self-healing cycles, the normalized  $\text{NO}_2$  sensitivity was changed by only 7.2% from its initial value. Similarly, Fig. 6e also verifies that repeated cycles of bisection and subsequent self-healing do not significantly degrade the performance of the multifunctional sensor for detecting UV light. After 5 cycles of self-healing process, the normalized UV sensitivity was changed by only 2.4% from its initial value. In addition to the stable operation of the sensor with the integrated supercapacitor, these results suggest that the multifunctional sensor exhibits self-healing properties owing to the self-healing PVA/agarose hydrogel substrate, similar to that demonstrated for the self-healing behavior of the supercapacitor. The cross-sectional SEM and optical images taken from the healed area of the fabricated multifunctional sensor are shown in Fig. S14. Finally, we measured the increase of photocurrent with increase of UV intensity from 0.4 to  $0.8 \text{ mWcm}^{-2}$  as shown in Fig. S15a. The photosensitivity is also given in Fig. S15b.

### 3. Conclusion

We demonstrated a fully self-healable all-in-one system of a planar supercapacitor and a multifunctional sensor integrated with AuNS interconnections, via a facile vacuum filtration technique. By using a rationally designed rapid self-healing hydrogel electrolyte with a high ionic conductivity, the high-performance self-healing planar supercapacitor could be fabricated to drive the integrated multifunctional sensor. Both the supercapacitor and the sensor could retain their

performance over repetitive cycles of bisectional damage and self-healing. This work suggests the high potential application of our self-healing devices to future wearable electronics with high durability and longevity.

### 4. Experimental section

**Materials:** Polyvinyl alcohol (PVA, average Mw 130,000), agarose (Bioreagent, low EEO), sodium tetraborate ( $\text{Na}_2\text{B}_4\text{O}_7$ ), sodium nitrate ( $\text{NaNO}_3$ ), zinc oxide nanowires (ZnO NWs, length: 20 nm, diameter:  $1 \mu\text{m}$ ), L-arginine ( $\geq 99.9\%$ ), and gold(III) chloride trihydrate ( $\geq 99.9\%$ ) ( $\text{HAuCl}_4 \cdot 3\text{H}_2\text{O}$ ) were purchased from Sigma Aldrich. All reagents were used without purification.

**Preparation of the self-healing hydrogel electrolyte:** To prepare the self-healing polymer electrolyte, 20 wt% of PVA and 1–3 wt% of agarose were first mixed with 4 ml DI water and stirred at  $120 \text{ }^\circ\text{C}$  for 4 h, forming a viscous solution. After cooling the prepared solution to  $90 \text{ }^\circ\text{C}$ , 2 ml of Sodium Nitrate solution ( $4 \text{ mol L}^{-1}$ ) was added and stirred continuously for 2 h. Finally, 2 ml of sodium tetraborate solution ( $0.04 \text{ mol L}^{-1}$ ) was slowly added dropwise and stirred for 1 h at  $90 \text{ }^\circ\text{C}$ . After cooling the hydrogel electrolyte to room temperature, it was put in a stainless mold and then pressed with a 2 kg weight for 1 h. The molding process was used to remove remaining bubbles and heal unwanted cracks in the hydrogel.

**Fabrication of gold nanosheets (AuNSs):** To synthesize the AuNSs, 10 ml of a  $1.95 \text{ mM}$  L-arginine solution was heated to  $95 \text{ }^\circ\text{C}$ , and 4 ml of a  $17 \text{ mM}$   $\text{HAuCl}_4 \cdot 3\text{H}_2\text{O}$  solution was added. The synthesis continued for 24 h. After cooling the AuNS suspension to room temperature, the liquid solution was replaced with 4 ml of ethanol while leaving the precipitated AuNSs in the vial.

**Fabrication of the self-healing all-in-one system:** A supercapacitor electrode was fabricated using a patterned PDMS via vacuum filtration. To prepare the PDMS mask, 1.0 g of PDMS base (Dow Corning, Sylgard 184A) and 0.1 g of curing agent (Dow Corning, Sylgard 184B) were mixed together, poured into plastic petri dish (diameter 55 mm), and then cured in an oven for 30 min at  $65 \text{ }^\circ\text{C}$ . The pattern was cut off using

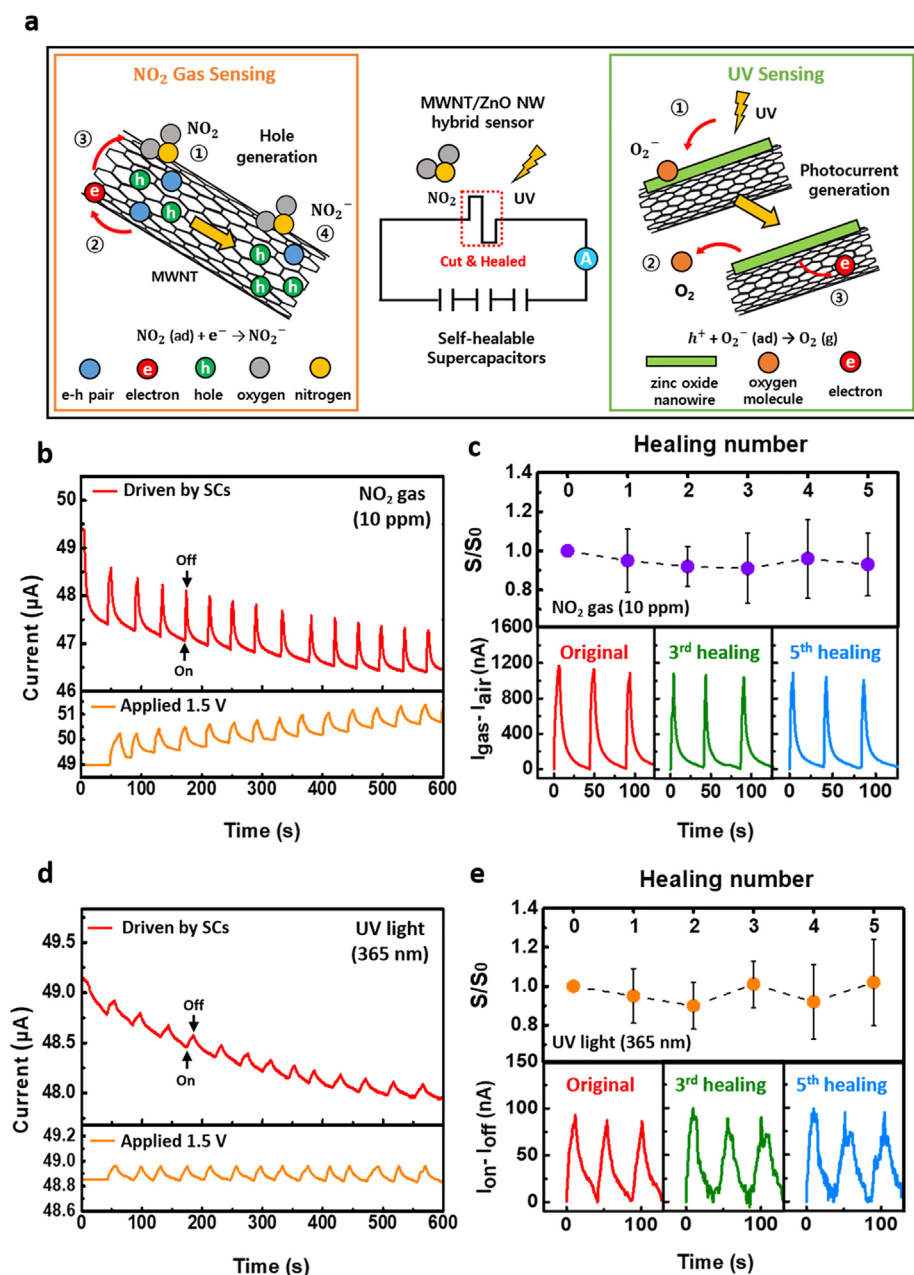


**Fig. 6.** (a) Schematic illustration of the sensing mechanism of the fabricated multi-functional sensor. (b) Change in the current upon periodic exposure to 10 ppm NO<sub>2</sub> driven by the SC array (top) and an external power supply of 1.5 V (bottom). (c) Normalized sensitivity ( $S/S_0$ ) with 5 cycles of self-healing. Bottom figure shows the change in the current over repetitive self-healing of the sensor. (d) Change in photocurrent upon periodic irradiation of 365 nm UV light with a sensor driven by the SC array (top) and an external power supply of 1.5 V (bottom). (e) Normalized sensitivity ( $S/S_0$ ) with 5 cycles of self-healing. Bottom figure shows the change in the photocurrent after repetitive self-healing of the sensor.

a razor blade. The patterned PDMS mask was placed on top of PTFE-T filter paper (pore size 0.2 μm, Hyundai Micro, Korea). For supercapacitor electrodes, 2 ml of the MWCNT dispersion and 2 ml of the synthesized AuNS dispersion were drop-cast sequentially. For multi-functional sensor, 0.1 ml of ZnO NW (0.5 mg ml<sup>-1</sup>) and 0.2 ml of MWCNT (1 mg ml<sup>-1</sup>) dispersion were also drop-cast. To detect both UV light and NO<sub>2</sub> gas, we deposited ZnO NWs on half of the sensor. Finally, AuNS dispersion was dropped to form interconnections. After patterning, sufficient DI water was dropped to remove the remaining solvent. Then, the PDMS mask was peeled off, and the sample was dried under vacuum conditions for 30 min. After drying, the filter paper with a patterned circuit was flipped upside down and laid on a PVA/agarose solution prepared on a Si/SiO<sub>2</sub> substrate. The PVA/agarose solution was prepared by dissolving 10 wt% of PVA and 1–3 wt% of agarose with DI water. After being dried on a 55 °C hot plate for 4 h, the filter paper was slowly peeled off. Then, the pattern transferred to the PVA/agarose substrate was also peeled off from the Si/SiO<sub>2</sub> substrate using a razor blade. Finally, the fabricated hydrogel electrolyte was simply placed on

the supercapacitor electrode.

**Characterization:** To measure the stress-stress curves of the hydrogel, a force sensor (Mark-10 Series 7, ± 0.1% accuracy) and motion controller (SM4-0806-3S) were operated with a custom-built LabVIEW program. The electrochemical properties of the supercapacitor were measured with a 2-electrode cell using an electrochemical analyzer (Ivium Technologies, Compact Stat). Time-dependent resistance change of the supercapacitor electrode was measured using a probe station (Agilent Technologies B1500A). The surface and cross-sectional morphologies of the MWCNTs, AuNSs, and ZnO NWs were obtained using SEM (Hitach S-4800).

#### CRediT authorship contribution statement

**Min Su Kim:** . **Jung Wook Kim:** Conceptualization, Writing - review & editing, Formal analysis. **Junyeong Yun:** Conceptualization, Methodology. **Yu Ra Jeong:** Formal analysis, Investigation. **Sang Woo Jin:** Formal analysis, Investigation. **Geumbee Lee:** Investigation.

**Hanchan Lee:** Investigation. **Dong Sik Kim:** Data curation. **Kayeon Keum:** Data curation, Writing - review & editing. **Jeong Sook Ha:** .

## Acknowledgments

This work was supported by the National Research Foundation of Korea (NRF) grant funded by the Korean government (MSIP) (Grant No. NRF-2019R1A2B5B03069545). It was also supported by a Korea University Grant. The authors also thank the KU-KIST graduate school program of Korea University.

## Declaration of Competing Interest

The authors declare no conflict of interest.

## Appendix A. Supplementary material

Supplementary data to this article can be found online at <https://doi.org/10.1016/j.apsusc.2020.146018>.

## References

- W. Li, X. Xu, C. Liu, M.C. Tekell, J. Ning, J. Guo, J. Zhang, D. Fan, Ultralight and binder-free all-solid-state flexible supercapacitors for powering wearable strain sensors, *Adv. Funct. Mater.* 27 (2017) 1702738.
- Y. Huang, S.V. Kershaw, Z. Wang, Z. Pei, J. Liu, Y. Huang, H. Li, M. Zhu, A.L. Rogach, C. Zhi, Highly integrated supercapacitor-sensor systems via material and geometry design, *Small* 12 (2016) 3393–3399.
- S. Jung, J. Lee, T. Hyeon, M. Lee, D.-H. Kim, Fabric-based integrated energy devices for wearable activity monitors, *Adv. Mater.* 26 (2014) 6329–6334.
- D. Yu, K. Goh, Q. Zhang, L. Wei, H. Wang, W. Jiang, Y. Chen, Controlled functionalization of carbonaceous fibers for asymmetric solid-state micro-supercapacitors with high volumetric energy density, *Adv. Mater.* 26 (2014) 6790–6797.
- T.-H. Kim, C.-S. Lee, S. Kim, J. Hur, S. Lee, K.W. Shin, Y.-Z. Yoon, M.K. Choi, J. Yang, D.-H. Kim, T. Hyeon, S. Park, S. Hwang, Fully stretchable optoelectronic sensors based on colloidal quantum dots for sensing photoplethysmographic signals, *ACS Nano* 11 (2017) 5992–6003.
- J.H. Koo, S. Jeong, H.J. Shim, D. Son, J. Kim, D.C. Kim, S. Choi, J.-I. Hong, D.-H. Kim, Wearable electrocardiogram monitor using carbon nanotube electronics and Color-Tunable organic light-emitting diodes, *ACS Nano* 11 (2017) 10032–10041.
- M.K. Choi, J. Yang, D.C. Kim, Z. Dai, J. Kim, H. Seung, V.S. Kale, S.J. Sung, C.R. Park, N. Lu, T. Hyeon, D.-H. Kim, Extremely vivid, highly transparent, and ultrathin quantum dot light-emitting diodes, *Adv. Mater.* 30 (2018) 1703279.
- P. Gutruf, V. Krishnamurthi, A. Vázquez-Guardado, Z. Xie, A. Banks, C.-J. Su, Y. Xu, C.R. Haney, E.A. Waters, I. Kandela, S.R. Krishnan, T. Ray, J.P. Leshock, Y. Huang, D. Chanda, J.A. Rogers, Fully implantable optoelectronic systems for battery-free, multimodal operation in neuroscience research, *Nat. Electron.* 1 (2018) 652–660.
- W.-P. Chen, D.-Z. Hao, W.-J. Hao, X.-L. Guo, L. Jiang, Hydrogel with ultrafast self-healing property both in air and underwater, *ACS Appl. Mater. Interfaces* 10 (2018) 1258–1265.
- Z. Wang, Q. Pan, An omni-healable supercapacitor integrated in dynamically cross-linked polymer networks, *Adv. Funct. Mater.* 27 (2017) 1700690.
- Z. Gong, G. Zhang, X. Zeng, J. Li, G. Li, W. Huang, R. Sun, C. Wong, High-strength, tough, fatigue resistant, and self-healing hydrogel based on dual physically cross-linked network, *ACS Appl. Mater. Interfaces* 8 (2016) 24030–24037.
- Y. Huang, M. Zhong, Y. Huang, M. Zhu, Z. Pei, Z. Wang, Q. Xue, X. Xie, C. Zhi, A self-healable and highly stretchable supercapacitor based on a dual crosslinked polyelectrolyte, *Nat. Commun.* 6 (2015) 10310.
- K.S. Toohy, N.R. Sottos, J.A. Lewis, J.S. Moore, S.R. White, Self-healing materials with microvascular networks, *Nat. Mater.* 6 (2007) 581–585.
- H. Wang, B. Zhu, W. Jiang, Y. Yang, W.R. Leow, H. Wang, X. Chen, A mechanically and electrically self-healing supercapacitor, *Adv. Mater.* 26 (2014) 3638–3643.
- Y. Yue, N. Liu, Y. Ma, S. Wang, W. Liu, C. Luo, H. Zhang, F. Cheng, J. Rao, X. Hu, J. Su, Y. Gao, Highly self-healable 3D microsupercapacitor with MXene-graphene composite aerogel, *ACS Nano* 12 (2018) 4224–4232.
- Y. Yang, X. Lu, W. Wang, A tough polyurethane elastomer with self-healing ability, *Mater. Des.* 127 (2017) 30–36.
- M. Nakahata, Y. Takashima, H. Yamaguchi, A. Harada, Redox-responsive self-healing materials formed from host-guest polymers, *Nat. Commun.* 2 (2011) 511.
- Y.-G. Jia, X.X. Zhu, Self-healing supramolecular hydrogel made of polymers bearing cholic acid and  $\beta$ -cyclodextrin pendants, *Chem. Mat.* 27 (2015) 387–393.
- X. Li, H. Zhang, P. Zhang, Y. Yu, A Sunlight-degradable autonomous self-healing supramolecular elastomer for flexible electronic devices, *Chem. Mat.* 30 (2018) 3752–3758.
- G. Cai, J. Wang, K. Qian, J. Chen, S. Li, P.S. Lee, Extremely stretchable strain sensors based on conductive self-healing dynamic cross-links hydrogels for human-motion detection, *Adv. Sci.* 4 (2017) 1600190.
- Y. He, S. Liao, H. Jia, Y. Cao, Z. Wang, Y. Wang, A self-healing electronic sensor based on thermal-sensitive fluids, *Adv. Mater.* 27 (2015) 4622–4627.
- Y. Wang, R. Zheng, J. Luo, H.A. Malik, Z. Wan, C. Jia, X. Weng, J. Xie, L. Deng, X. Yao, Self-healing dynamically cross linked versatile polymer electrolyte: A novel approach towards high performance, flexible electrochromic devices, *Electrochim. Acta.* 320 (2019) 134489.
- G. Liang, Z. Liu, F. Mo, Z. Tang, H. Li, Z. Wang, V. Sarangi, A. Pramanick, J. Fan, C. Zhi, Self-healable electroluminescent devices, *Light Sci. Appl.* 7 (2018) 102.
- Y. Shi, Y. Zhang, L. Jia, Q. Zhang, X. Xu, Stretchable and self-healing integrated all-gel-state supercapacitors enabled by a notch-insensitive supramolecular hydrogel electrolyte, *ACS Appl. Mater. Interfaces* 10 (2018) 36028–36036.
- F. Liu, J. Wang, Q. Pan, An all-in-one self-healable capacitor with superior performance, *J. Mater. Chem. A* 6 (2018) 2500–2506.
- J. Wang, F. Liu, F. Tao, Q. Pan, Rationally designed self-healing hydrogel electrolyte toward a smart and sustainable supercapacitor, *ACS Appl. Mater. Interfaces* 9 (2017) 27745–27753.
- F. Tao, L. Qin, Z. Wang, Q. Pan, Self-healable and cold-resistant supercapacitor based on a multifunctional hydrogel electrolyte, *ACS Appl. Mater. Interfaces* 9 (2017) 15541–15548.
- D. Son, J. Kang, O. Vardoulis, Y. Kim, N. Matsuhisa, J.Y. Oh, J.W.F. To, J. Mun, T. Katsumata, Y. Liu, A.F. McGuire, M. Krason, F. Molina-Lopez, J. Ham, U. Kraft, Y. Lee, Y. Yun, J.B.H. Tok, Z. Bao, An integrated self-healable electronic skin system fabricated via dynamic reconstruction of a nanostructured conducting network, *Nat. Nanotechnol.* 13 (2018) 1057–1065.
- H. Fei, C. Yang, H. Bao, G. Wang, Flexible all-solid-state supercapacitors based on graphene/carbon black nanoparticle film electrodes and cross-linked poly(vinyl alcohol)-H<sub>2</sub>SO<sub>4</sub> porous gel electrolytes, *J. Power Sources* 266 (2014) 488–495.
- C. Zhao, C. Wang, Z. Yue, K. Shu, G.G. Wallace, Intrinsically stretchable supercapacitors composed of polypyrrole electrodes and highly stretchable gel electrolyte, *ACS Appl. Mater. Interfaces* 5 (2013) 9008–9014.
- C.-C. Yang, S.-J. Lin, S.-T. Hsu, Synthesis and characterization of alkaline polyvinyl alcohol and poly(epichlorohydrin) blend polymer electrolytes and performance in electrochemical cells, *J. Power Sources* 122 (2003) 210–218.
- G. Ma, J. Li, K. Sun, H. Peng, J. Mu, Z. Lei, High performance solid-state supercapacitor with PVA-KOH-K<sub>3</sub>[Fe(CN)<sub>6</sub>] gel polymer as electrolyte and separator, *J. Power Sources* 256 (2014) 281–287.
- M. Jiang, J. Zhu, C. Chen, Y. Lu, Y. Ge, X. Zhang, Poly(vinyl alcohol) borate gel polymer electrolytes prepared by electrodeposition and their application in electrochemical supercapacitors, *ACS Appl. Mater. Interfaces* 8 (2016) 3473–3481.
- N. Batisse, E. Raymundo-Piñero, A self-standing hydrogel neutral electrolyte for high voltage and safe flexible supercapacitors, *J. Power Sources* 348 (2017) 168–174.
- A. Bhattacharya, P. Ray, Studies on surface tension of poly(vinyl alcohol): Effect of concentration, temperature, and addition of chaotropic agents, *J. Appl. Polym. Sci.* 93 (2004) 122–130.
- S. Patachia, C. Florea, C. Friedrich, Y. Thomann, Tailoring of poly(vinyl alcohol) cryogels properties by salts addition, *Express Polym. Lett.* 3 (2009) 320–331.
- B. Briscoe, P. Luckham, S. Zhu, The effects of hydrogen bonding upon the viscosity of aqueous poly(vinyl alcohol) solutions, *Polymer* 41 (2000) 3851–3860.
- Z. Wang, F. Tao, Q. Pan, A self-healable polyvinyl alcohol-based hydrogel electrolyte for smart electrochemical capacitors, *J. Mater. Chem. A* 4 (2016) 17732–17739.
- S.W. Sinton, Complexation chemistry of sodium borate with poly(vinyl alcohol) and small diols: a boron-11 NMR study, *Macromolecules* 20 (1987) 2430–2441.
- R.K. Schultz, R.R. Myers, The chemorheology of poly(vinyl alcohol)-borate gels, *Macromolecules* 2 (1969) 281–285.
- Q. Chen, L. Zhu, C. Zhao, Q. Wang, J. Zheng, A. Robust, One-pot synthesis of highly mechanical and recoverable double network hydrogels using thermoreversible sol-gel polysaccharide, *Adv. Mater.* 25 (2013) 4171–4176.
- H. Chen, Q. Chen, R. Hu, H. Wang, B.-m.Z. Newby, Y. Chang, J. Zheng, Mechanically strong hybrid double network hydrogels with antifouling properties, *J. Mater. Chem. B*, 3 (2015) 5426–5435.
- T.J. Trivedi, D. Bhattacharjya, J.-S. Yu, A. Kumar, Functionalized agarose self-healing ionogels suitable for supercapacitors, *ChemSusChem* 8 (2015) 3294–3303.
- M. Sabzi, N. Samadi, F. Abbasi, G.R. Mahdavinia, M. Bahaahmadi, Bioinspired fully physically cross-linked double network hydrogels with a robust, tough and self-healing structure, *Mater. Sci. Eng. C* 74 (2017) 374–381.
- H.S. Mansur, C.M. Sadahira, A.N. Souza, A.A.P. Mansur, FTIR spectroscopy characterization of poly(vinyl alcohol) hydrogel with different hydrolysis degree and chemically crosslinked with glutaraldehyde, *Mater. Sci. Eng. C* 28 (2008) 539–548.
- M. Tako, M. Higa, K. Medoruma, Y. Nakasone, A highly methylated agar from red seaweed, *Gracilaria arcuata*, *Bot. Mar.* (1999) 513.
- J.G. Lyons, L.M. Geever, M.J.D. Nugent, J.E. Kennedy, C.L. Higginbotham, Development and characterisation of an agar-polyvinyl alcohol blend hydrogel, *J. Mech. Behav. Biomed.* 2 (2009) 485–493.
- N.A. Peppas, Infrared spectroscopy of semicrystalline poly(vinyl alcohol) networks, *178 (1977) 595–601*.
- M. Huang, Y. Hou, Y. Li, D. Wang, L. Zhang, High performances of dual network PVA hydrogel modified by PVP using borax as the structure-forming accelerator, *Des. Monomers. Polym.* 20 (2017) 505–513.
- Y. Zhang, P.S. Cremer, Interactions between macromolecules and ions: the Hofmeister series, *Curr. Opin. Chem. Biol.* 10 (2006) 658–663.
- E. Thormann, On understanding of the Hofmeister effect: how addition of salt alters the stability of temperature responsive polymers in aqueous solutions, *RSC Adv.* 2 (2012) 8297–8305.
- A.M. Hyde, S.L. Zultanski, J.H. Waldman, Y.-L. Zhong, M. Shevlin, F. Peng, General principles and strategies for salting-out informed by the Hofmeister series, *Org.*

- Process Res. Dev. 21 (2017) 1355–1370.
- [53] Z. Yang, Hofmeister effects: an explanation for the impact of ionic liquids on biocatalysis, *J. Biotechnol.* 144 (2009) 12–22.
- [54] B.-A. Mei, O. Munteshari, J. Lau, B. Dunn, L. Pilon, Physical interpretations of Nyquist plots for EDLC electrodes and devices, *J. Phys. Chem. C* 122 (2018) 194–206.
- [55] R. Jia, L. Li, Y. Ai, H. Du, X. Zhang, Z. Chen, G. Shen, Self-healable wire-shaped supercapacitors with two twisted NiCo<sub>2</sub>O<sub>4</sub> coated polyvinyl alcohol hydrogel fibers, *Sci. China Mater.* 61 (2018) 254–262.
- [56] H. Zhou, H. Luo, X. Zhou, H. Wang, Y. Yao, W. Lin, G. Yi, Healable, Flexible Supercapacitors Based on Shape Memory Polymers 8 (2018) 1732.
- [57] G. Li, L. Gao, L. Li, L. Guo, An electrochromic and self-healing multi-functional supercapacitor based on PANI/nw-WO<sub>2.7</sub>/Au NPs electrode and hydrogel electrolyte, *J. Alloy. Compd.* 786 (2019) 40–49.
- [58] X. Liang, L. Zhao, Q. Wang, Y. Ma, D. Zhang, A dynamic stretchable and self-healable supercapacitor with a CNT/graphene/PANI composite film, *Nanoscale* 10 (2018) 22329–22334.
- [59] D.R. Kumar, D. Manoj, J. Santhanalakshmi, Au–ZnO bullet-like heterodimer nanoparticles: synthesis and use for enhanced nonenzymatic electrochemical determination of glucose, *RSC Adv.* 4 (2014) 8943–8952.
- [60] J. Das, S.K. Pradhan, D.R. Sahu, D.K. Mishra, S.N. Sarangi, B.B. Nayak, S. Verma, B.K. Roul, Micro-Raman and XPS studies of pure ZnO ceramics, *Phys. B* 405 (2010) 2492–2497.
- [61] H. Zhou, Z. Li, Synthesis of nanowires, nanorods and nanoparticles of ZnO through modulating the ratio of water to methanol by using a mild and simple solution method, *Mater. Chem. Phys.* 89 (2005) 326–331.
- [62] W.-S. Cho, S.-I. Moon, K.-K. Paek, Y.-H. Lee, J.-H. Park, B.-K. Ju, Patterned multi-wall carbon nanotube films as materials of NO<sub>2</sub> gas sensors, *Sensor Actuat. B-Chem.* 119 (2006) 180–185.
- [63] J.H. Lee, Y. Seo, Y.D. Park, J.E. Anthony, D.H. Kwak, J.A. Lim, S. Ko, H.W. Jang, K. Cho, W.H. Lee, Effect of crystallization modes in TIPS-pentacene/insulating polymer blends on the gas sensing properties of organic field-effect transistors, *Sci. Rep.* 9 (2019) 21.
- [64] C. Song, J. Yun, H. Lee, H. Park, Y.R. Jeong, G. Lee, M.S. Kim, J.S. Ha, A Shape memory high-voltage supercapacitor with asymmetric organic electrolytes for driving an integrated NO<sub>2</sub> gas sensor, *Adv. Funct. Mater.* 29 (2019) 1901996.
- [65] J.H. Bang, K.S. Suslick, Applications of ultrasound to the synthesis of nanostructured materials, *Adv. Mater.* 22 (2010) 1039–1059.
- [66] X. Geng, L. Niu, Z. Xing, R. Song, G. Liu, M. Sun, G. Cheng, H. Zhong, Z. Liu, Z. Zhang, L. Sun, H. Xu, L. Lu, L. Liu, Aqueous-processable noncovalent chemically converted graphene-quantum dot composites for flexible and transparent optoelectronic films, *Adv. Mater.* 22 (2010) 638–642.
- [67] J.D. Fowler, M.J. Allen, V.C. Tung, Y. Yang, R.B. Kaner, B.H. Weiller, Practical chemical sensors from chemically derived graphene, *ACS Nano* 3 (2009) 301–306.
- [68] F. Schedin, A.K. Geim, S.V. Morozov, E.W. Hill, P. Blake, M.I. Katsnelson, K.S. Novoselov, Detection of individual gas molecules adsorbed on graphene, *Nat. Mater.* 6 (2007) 652–655.